Enhanced Strain in Functional Nanoporous Gold with a Dual Microscopic Length Scale Structure

Eric Detsi, Sergey Punzhin, Jiancun Rao, Patrick R. Onck, and Jeff Th. M. De Hosson*

Department of Applied Physics, Zernike institute for Advanced Materials and Materials Innovation Institute M2i, University of Groningen, Nijenborgh 4, 9747 AG Groningen, The Netherlands

ABSTRACT

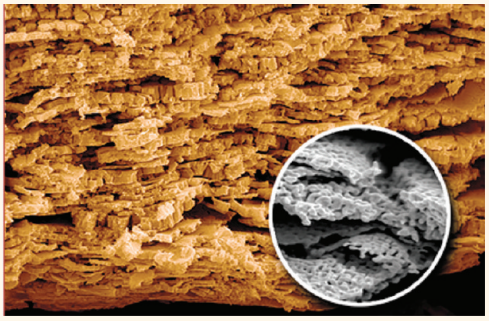

We have synthesized nanoporous Au with a dual microscopic length scale by exploiting the crystal structure of the alloy precursor. The synthesized mesoscopic material is characterized by stacked Au layers of submicrometer thickness. In addition, each layer displays nanoporosity through the entire bulk. It is shown that the thickness of these layers can be tailored *via* the grain size of the alloy precursor. The two-length-scale structure enhances the functional properties of nanoporous gold, leading to charge-induced strains of amplitude up to 6%, which are roughly 2 orders of magnitude larger than in nanoporous Au with the standard one-length-scale porous morphology. A model is presented to describe these phenomena.

KEYWORDS: nanoporous metals · stacked porous layers charge-induced strain · actuator · sensor

In recent years nanoporous metals have attracted considerable attention due to their potential for various applications, including catalysts, sensors, actuators, supercapacitors, nanofilters, and drug delivery platforms.[1−15] Dealloying, *i.e.*, a corrosion process during which the less noble alloy component is selectively etched away, is a commonly used method for the synthesis of nanoporous metals.[1−10,13−30] During the dealloying process, ligament and pore sizes can be tailored by (i) tuning the ratio of the alloy precursor elements; *e.g.*, for a Au−Ag binary system, ligament and pore sizes decrease with increasing silver content in the alloy;[20,21] and (ii) tuning the dealloying parameters; *e.g.*, for the same binary system, ligament and pore sizes decrease with increasing dealloying potential.[23] Also the electrolyte temperature has been exploited to control the structure size, and the size of ligaments and pores decreases with decreasing electrolyte temperature.[25] (iii) Finally, ligament and pore sizes can be controlled by post-dealloying treatments. During this process a dealloyed material is either kept in acid[26] or exposed to high temperatures[27,28] to induce coarsening of the ligaments.

Downscaling the size of ligaments and pores to smaller dimensions is particularly interesting because material properties associated with bulk nanoporous metals are enhanced when ligament and pore sizes decrease.[22−29] Obviously, the size of microstructural elements cannot be scaled down indefinitely. Therefore, alternative porous structures are desirable in order to improve the functional properties of nanoporous materials. In this paper, we show that nanoporous Au with a dual microstructural length scale can be synthesized by exploiting the crystal structure of the alloy precursor. Further, we show that this multiscale structure enhances the physical properties of nanoporous materials. This is done by investigating the charge-induced strain response of the synthesized nanoporous Au and by comparing this response to that of nanoporous Au with the standard porous morphology.

Nanoporous Au was synthesized by free corrosion of the $Au_5Pd_{20}Ag_{75}$ (at. %) ternary alloy precursor in 32% nitric acid and at room temperature (see Supporting Information for the synthesis of the starting alloy). During the free corrosion process, Ag and Pd are selectively leached out of the precursor. The motivation for the usage of a ternary system as precursor rather than the standard Au−Ag binary alloy is discussed later. Prior to dealloying, the starting alloy

* Address correspondence to j.t.m.de.hosson@rug.nl.

Received for review November 5, 2011 and accepted March 31, 2012.

Published online March 31, 2012
10.1021/nn300179n

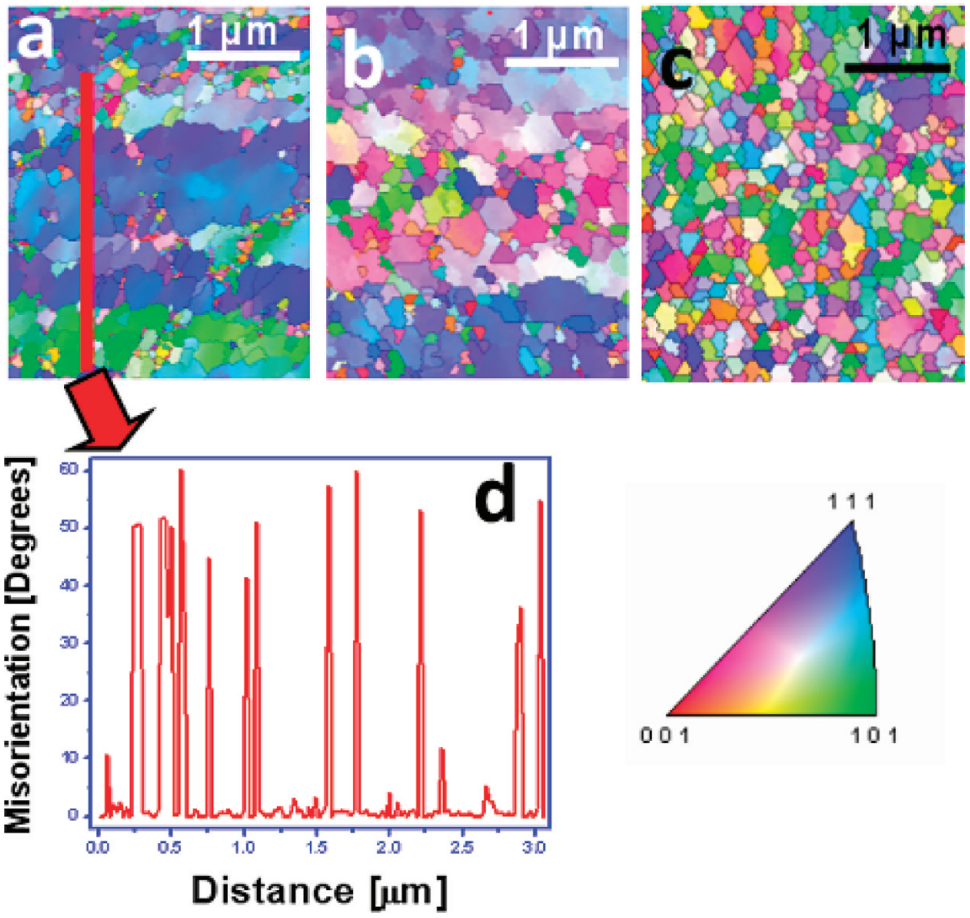

Figure 1. Grain boundary texture in the alloy precursors. (a) Orientation map based on the [001] inverse pole figure of the Au–Pd–Ag precursor with cold-rolled thickness 250 μm, annealed at low temperatures. The microband texture of the cold-rolled grains can be distinguished. This texture is characterized by the preferential orientation of the elongated grains in the [111] (blue and purples grains) and [101] (green grains) directions. (b) Orientation map based on the [001] inverse pole figure of the precursor with cold-rolled thickness 500 μm, annealed at low temperatures. Orientation of the microband groups in the [111] and [001] directions can be distinguished. (c) Orientation map based on the [001] inverse pole figure of the precursor with cold-rolled thickness 250 μm, annealed at high temperatures. The microband texture vanishes during recrystallization. (d) Misorientation profile of the grains from (a), obtained from TSL-OIM analysis. Higher misorientation angles (higher peaks) are associated with the elongated grains.

was subjected to the following two treatments: (i) cold-rolling from the initial thickness of ~5 mm down to sub-millimeter thicknesses and (ii) heat treatments at low temperature (*e.g.*, 350 °C for maximum 24 h) or at high temperature (*e.g.*, 700 °C for maximum 7 h). Rectangular samples with sizes 2 × 1 × 0.25 mm^3 and 2 × 1 × 0.5 mm^3 were obtained from the cold-rolled and heat-treated samples for dealloying.

RESULTS AND DISCUSSION

Microstructural Characterization of the Alloy Precursor. The microstructures of the cold-rolled and heat-treated alloy precursors were investigated using electron backscatter diffraction (EBSD), FEI XL30 SEM FEG. Figure 1a and b display orientation maps based on the [001] inverse pole figure of the cross-section of two cold-rolled alloy precursors with thickness 250 and 500 μm, respectively. These two starting alloys were annealed at low temperatures. Figure 1c displays an orientation map based on the [001] inverse pole figure of an alloy precursor with thickness 250 μm, annealed at high temperature. Figure 1d represents a typical grain misorientation profile as obtained from TSL-OIM analysis. The misorientation profile is measured along a vertical direction, as illustrated by the red line in Figure 1a. The horizontal axis in Figure 1d indicates the distance, and the vertical axis represents the misorientation angle along the line.

A preferential orientation is observed in EBSD analysis (Figure 1a and b). Grains orientation in the [111] and [101] directions for Figure 1a and in the [111] and [001] directions for Figure 1b can clearly be distinguished. In contrast, grains appear to be randomly oriented in cold-rolled samples when heat treated at high temperature (Figure 1c). Recovery and recrystallization occur at higher temperatures.

Grains in the alloy precursors subjected to low-temperature annealing are oriented in microbands (see Figure 1a and b). The average density in the microband texture of the sample with initial thickness

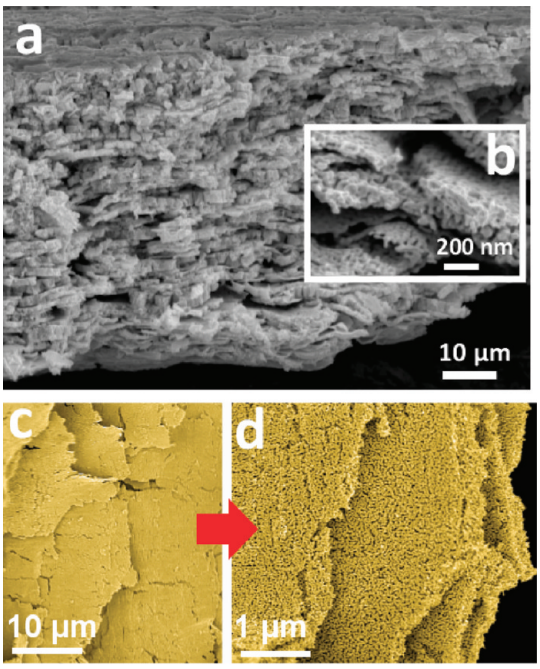

Figure 2. (a–d) Fracture cross sections of nanoporous Au showing stacked porous layers at different magnifications. These layered structures are obtained from the alloy precursor in Figure 1a, and the density of the nanoporous Au layers through the cross section corresponds to that of the microband texture in the precursor in Figure 1a.

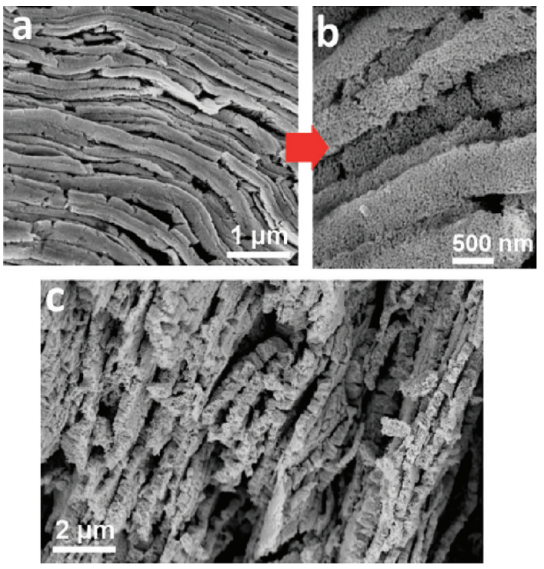

Figure 3. (a, b) Nonfracture and (c) fracture cross sections of nanoporous Au showing stacked porous layers at different magnifications. These layered structures are obtained from the alloy precursor in Figure 1b, and the density of the nanoporous Au layers through the cross section corresponds to that of the microband texture in the precursor in Figure 1b.

of 250 μm (Figure 1a) was found to be ~11 microbands along a 3.5 μm cross section (*i.e.*, ~3 per μm). This packing density can be deduced either from differences in color among microbands, as shown in Figure 1a, or from the density of high peaks in the corresponding grain misorientation profile, as illustrated in Figure 1d. In a similar way, the average density in the microband texture of the sample with initial thickness of 500 μm (Figures 1b) was found to be ~1 microband per μm.

The microband structure in the starting alloys is used as a precursor for the synthesis of nanoporous Au with a dual microscopic length scale. Note that the Au–Pd–Ag ternary system was preferred to the Au–Ag binary alloy because the grain orientation texture introduced in the Au–Ag alloy by cold-rolling was found to partially disappear during annealing. The microband texture is better preserved in the Au–Pd–Ag starting alloy under similar annealing conditions. A possible explanation for this might be the relatively higher recrystallization temperature of the Au–Pd–Ag ternary system compared to that of the Au–Ag binary alloy.

Dealloying Process. The free corrosion process was observed to be relatively slow compared to that of the binary alloy (about 20 times slower). At the end of the dealloying process, both gravimetric analysis and EDS were employed to verify that all Ag and Pd were etched away. Considerable volume shrinkage was observed after dealloying: the final volume of dealloyed samples represents only a ~20% volume fraction of the initial alloy precursor. This corresponds to 80% volume shrinkage. For comparison, volume contractions up to 30% have been reported[16] in nanoporous Au obtained from binary alloys with composition between $Au_{20}Ag_{80}$ and $Au_{33}Ag_{65}$ (at. %). Parida *et al.*[16] attributed this ~30% volume shrinkage to local plastic deformation taking place during dealloying. A very high density of crystal defects is indeed expected in our material if one takes into account the following two points: (i) the starting alloy was severely cold-rolled from its initial thickness of ~5 mm down to submillimeter thickness; (ii) the fraction of more noble element in the face-centered cubic (fcc) lattice of the alloy precursor is very low (only 5 at. %), which means that each Au atom has fewer other neighboring Au atoms.[19] This might favor the formation of defects in the crystal lattice when 95 at. % of material consisting of less noble elements (Ag, Pd) is etched away during dealloying.

The thickness of the cold-rolled ternary alloy was mostly affected during the volume shrinkage: after dealloying it decreases for about ~72% in the 250 μm thick samples (from 250 μm to ~70 μm) and ~40% in the 500 μm thick samples (from 500 μm to ~200 μm).

Microstructural Characterization of the Synthesized Nanoporous Au. Ultra-high-resolution scanning electron microscopy (UHR-SEM) FEI-XL30s SEM-FEG and high-resolution transmission electron microscopy (HRTEM) Jeol-JEM-2010F were employed to characterize the synthesized nanoporous Au. Stacked Au layers with submicrometer thicknesses are observed along the entire cross section of dealloyed samples whose

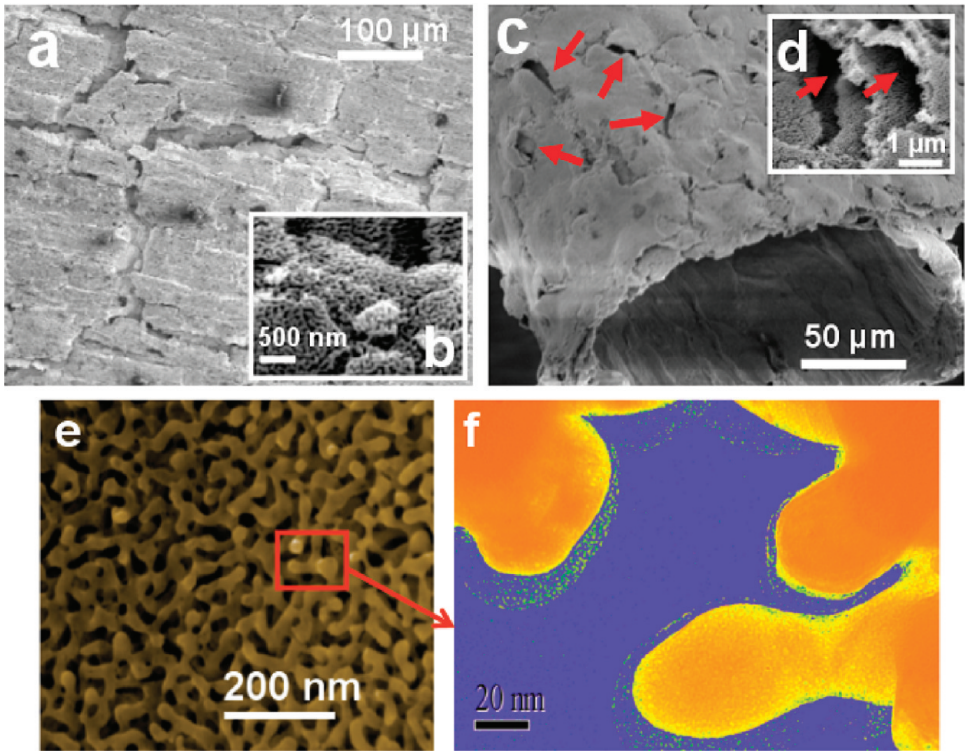

Figure 4. Scale morphology. (a) Undeformed surface. The layers are formed by scales with characteristic lateral dimension varying between ~10 and ~200 μm. (b) Higher magnification micrograph showing the porous structure of the scales. (c) Deformed surface. The scales are partially delaminated from the underlying layers. (d) At higher magnification it can be seen that the scales deformed by bending. (e) Ultra-high-resolution scanning electron micrograph showing the porous structure of a Au layer. The average ligament size is 30 nm. (f) False color transmission electron micrographs displaying individual Au ligaments covered by an oxide formed during the dealloying process.

precursors are heat treated at low temperature. Each of these layers displays nanoporosity through the entire bulk. The typical fracture cross sections of nanoporous Au obtained from the alloy precursor with 250 μm initial thickness are shown at different magnifications in Figure 2a–d. It can be seen that the microband texture in the alloy precursor as displayed in Figure 1a has given rise to nanoporous Au with a layered morphology. The scanning electron micrographs in Figure 3 represent both nonfracture (Figure 3a and b) and fracture (Figure 3c) cross sections of nanoporous Au samples obtained from the alloy precursor with 500 μm initial thickness. It is shown that the porous Au layers obtained from the alloy precursor with initial thickness 250 μm are more densely packed than those obtained from the alloy precursor with 500 μm initial thickness.

In order to quantitatively confirm the relation between the porous multilayer morphology and the microband texture in the precursors, the densities of the microbands as determined in the previous section were compared to those of the porous Au layers. About 700 nanoporous Au layers were estimated through the entire dealloyed cross section (*i.e.*, 70 μm) of the sample with an initial thickness of 250 μm. This corresponds to a packing density of ~10 nanoporous Au layers per μm. The corresponding alloy precursor displays ~11 microbands along a cross section with a length of 3.5 μm. Note that during dealloying, 3.5 μm decreases to 1 μm (~72% shrinkage). This means that the packing density of the microbands becomes ~11 per μm after dealloying, which corresponds to that of the porous layers. Similarly, when taking into account the ~40% shrinkage in the thicker sample (500 μm) during dealloying, we found that the packing density of the porous Au layers (~1.5 layer per μm) is comparable to that of the microbands, *i.e.*, ~1.5 microband per μm (note that it was ~2 microbands over 2 μm before dealloying). This confirms that the multilayer morphology in our nanoporous Au is directly coupled to the layered texture development in the alloy precursor.

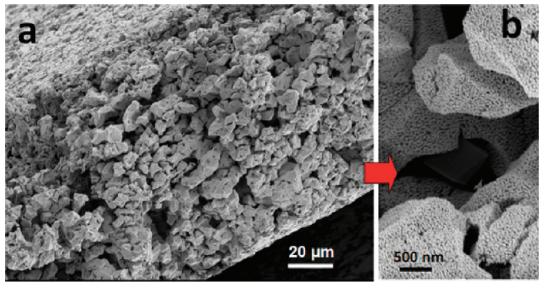

Figure 5. Grained architecture. (a) Fracture cross section of a dealloyed structure obtained from a cold-rolled precursor heat treated at high temperature (see Figure 1c). The nanoporous layered structure is not formed. Instead, nanoporous Au grains are formed. (b) Porosity of the grains at higher magnification.

SEM investigations of the porous multilayer morphology indicate that at a given plane the layers are not continuous. Rather, they form scales, as can be seen at different magnifications in Figure 4a to d (see also Figure 2c). The lateral characteristic dimension of the scales varies between ~10 and ~200 μm. These dimensions are comparable to the grain size distribution in the original alloy before cold rolling, which is in agreement with the fact that the scales come from flattened pancake grains (microbands). These scales are partially delaminated and also locally attached onto the underlying layers. The partial delamination of the scales can be clearly seen at lower magnification, *e.g.*, compare the structure of an undeformed sample (see Figure 4a) with that of a deformed sample (see Figure 4c and d). When a sample is deformed, the partial delamination of the scales is clearly visible, as indicated by the arrows in Figure 4c and d, where it can be seen that the scales deform by buckling. This deformation mode will be exploited to achieve giant macroscopic strains.

UHR-SEM investigations indicate that the nanoporous Au ligaments have an average diameter of ~30 nm (see Figure 4e). The TEM micrograph of the ligaments investigated using HRTEM (see Figure 4f) displays an oxide layer with an average thickness of 2 nm covering these ligaments. This thick oxide layer comes from Ag and Pd oxidation during the corrosion process,[30] and it was fully reduced during subsequent electrochemical treatments.[30]

The thickness of the layers in the novel structure can be controlled by tuning the thickness of the cold-rolled alloy precursor. The thickness of the nanoporous Au layers varies between ~50 and ~200 nm (see Figure 2) for the precursor with a cross-section of 250 μm (Figure 1a) and between ~450 and ~650 nm (see Figure 3) for the precursor with a cross-section of 500 μm (Figure 1b). Furthermore, if the microband texture is fully removed during heat treatments (see Figure 1c), the corresponding dealloyed structure does not display nanoporous Au layers. Rather, it displays nanoporous grains throughout the bulk cross section, as shown in Figure 5. Note that the average size of the nanoporous grains in Figure 5 is bigger than the average size of the grains in the recrystallized alloy precursor (Figure 1c). This suggests a local fusion of boundaries between adjacent grains during dealloying.[31]

Although it is evident that the porous layers in our dealloyed structure come from pancaked grains due to the cold-rolling process, an interesting question concerns the mechanism that governs the formation of these porous layers. Obviously, the cold-rolling process is key in our work. In order to systematically handle this question, we first consider the simple case of an alloy precursor that is not subjected to cold-rolling, and we find out whether this non-cold-rolled alloy also leads to a nanoporous structure with a two microscopic length scale like the structure displayed in Figure 5. In that structure, the average grain size corresponds to one length scale, and the size of ligaments and pores represents the other length scale. The two-length-scale morphology in our nanoporous Au is characterized by partially open boundaries between adjacent porous grains (or porous layers) throughout the entire bulk. This means that a two-length-scale structure can be obtained from a non-cold-rolled alloy precursor provided that the boundaries between adjacent grains remain partially open throughout the entire porous bulk during dealloying. In practice however, grain boundaries in non-cold-rolled dealloyed structures are only locally open, as reported by Sun and Balk.[31] This suggests that cold-rolling helps in producing partly open grain boundaries throughout the entire bulk during dealloying.

The origin of the locally open grain boundaries can be attributed[31] either to possible enrichment of the less noble alloy element at certain grain boundaries or to the ease/difficulty with which atoms diffuse along ground boundaries. In order to find out which of these two hypotheses is applicable to our system, we have investigated both phases present in our alloy precursors and their uniformity in chemical composition by X-ray diffraction and EDS, respectively. Our cold-rolled alloys display a homogeneous chemical composition, and it is concluded that the hypothesis concerning the enrichment of less noble elements at grain boundaries is less likely in our case. The physical origin of the open boundary morphology seems to point toward the second hypothesis[31] based on the ease/difficulty of atoms to diffuse along grain boundaries. This second assumption is compatible with the strong influence of the specific character of grain boundaries on the intergranular corrosion behavior in polycrystalline materials in general.[32] The corrosion activity at grain boundaries depends on the degree of misorientation between the neighboring grains. This means that, in comparison with our cold-rolled alloy precursors, large misorientations between adjacent microbands (see Figure 1d) do not favor fusion of the boundaries between adjacent microbands during dealloying. As a consequence, the resulting porous layers remain partially delaminated and also locally pinned onto each other during dealloying.

Electrochemical Characterization and Giant Reversible Strains. It has been shown that electric charge accumulated in the space-charge region at the metal surface during atom or anion adsorption from a gas or from an electrolyte strengthens (or weakens depending on the sign of the charge) the atomic bonds at the metal surface, giving rise to changes in the nanoporous metal surface stress. Due to the high surface-to-volume ratio of nanoporous metals, changes in the surface stress induce dimensional changes[6,7,9,10] known as charge-induced strains. In this paper we show a

significantly enhanced charge-induced strain response of nanoporous Au with the novel multilayer morphology. Electric charge injection in the space-charge region at the nanoporous Au interface is achieved during electrochemical formation of Au oxide.[33,34] During electrochemical oxidation (reduction) of Au, charge transferred *via* anion adsorption (desorption) gives rise to changes in the material surface stress as aforementioned and subsequently to dimensional changes.[6,7,9,10]

Since the oxidation (reduction) of Au was electrochemically achieved, it is necessary to perform electrochemical characterization of the material, prior to strain measurements. Electrochemical characterization is aimed at the following: (i) tuning the surface stress of the material through Au oxidation and reduction,; (ii) investigation of the reproducibility of this oxidation–reduction process; (iii) confirmation of the purity of the material (the EDS analysis provides only local information on the scanned surface area about the removal of the Pd and Ag after the dealloying process); and (iv) indirect investigation of the increase in the material specific surface area due to the layered structure and its possible implication for the giant macroscopic strains. A three-electrode electrochemical cell, containing 1 M perchloric acid, and a potentiostat (μAutolab III-FRA2, Eco Chemie) were used for the electrochemical characterization. Successive cyclic voltammetry experiments were performed in a potential range between 0.7 and 1.4 V with respect to a Ag/AgCl reference electrode, at a scan rate of 10 $mV \cdot s^{-1}$. During each scan, Au oxide formation (anodic scan) and reduction (cathodic scan) take place at the Au–electrolyte interface.[33,34] Cyclic voltammograms obtained conform to the well-known chemical signature of polycrystalline gold electrode[33,34] as displayed in Figure 6a, where 21 successive cyclic voltammograms are plotted. From Figure 6a and b it is concluded that these 21 voltammograms are perfectly reproducible. Furthermore, the fact that no irregular peaks are observed besides the expected Au oxidation and reduction peaks provides supplementary confirmation that both Pd and Ag are fully etched away from the Au–Pd–Ag alloy. The specific surface area of the material was indirectly investigated in the double-layer charging regime (see Supporting Information).[20] It was concluded that the increase in the specific surface area is not responsible for these giant strain amplitudes.

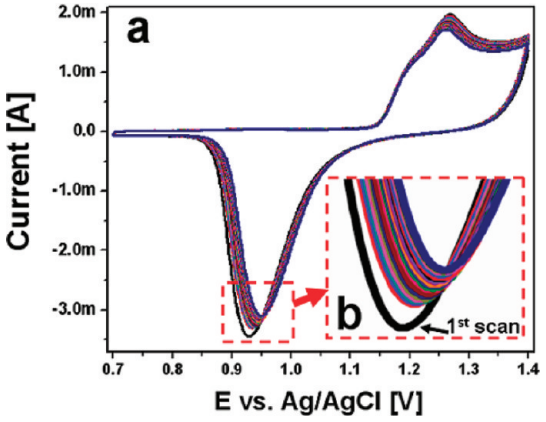

Figure 6. (a, b) Twenty-one successive cyclic voltammograms obtained during electrochemical characterization. These voltammograms are in conformity with the typical electrochemical signature of a polycrystalline Au electrode. The cathodic peak intensities gradually decrease due to the reduction of the oxide layer formed during the dealloying process.

Strain measurements were performed during similar cyclic voltammetry experiments. A confocal displacement sensor (IFS2401-0.4 Micro-Epsilon) was used *in situ* to probe the dimensional changes of the nanoporous samples (see Methods and Supporting Figure S1).[35] The typical input voltage as a function of the time is shown in Figure 7a. The corresponding output strain as a function of time is shown in Figure 7b. The current associated with the charge transfer activity at the nanoporous

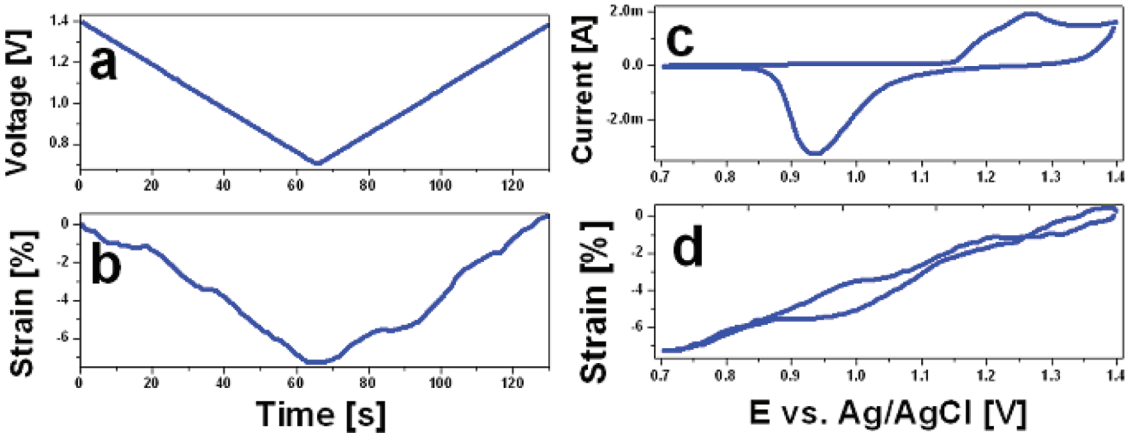

Figure 7. Charge-induced strain measurements. (a) Applied voltage as a function of time for a single cycle. (b) Corresponding strain as a function of time. (c) Current and (d) strain as a function of voltage. A linear dependence of the charge-induced strain on the voltage is observed together with hysteresis regions. These hysteresis regions overlap with the hysteresis regions on the current–voltage characteristic.

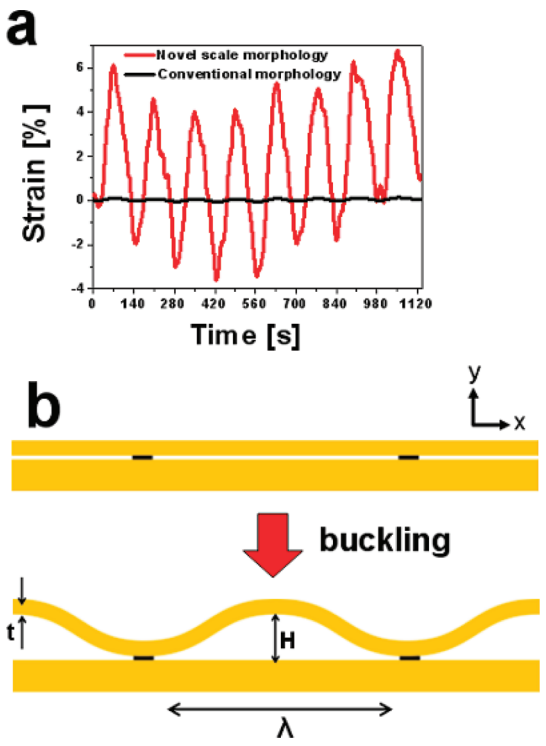

Figure 8. Giant reversible strains. (a) Red curve: Giant strain amplitudes up to 6% are measured on nanoporous Au with scale morphology. Black curve: Strain amplitudes of 0.1% are measured on the conventional nanoporous Au. (b) Deflection of the scales during deformation. The deformed scale profile was approximated with a wave function.

Au/electrolyte interface and the corresponding charge-induced strain are plotted as a function of the voltage in Figure 7c and d. A linear dependence of the charge-induced strain on the voltage is observed together with hysteresis (Figure 7d). These sections of hysteresis in the strain−voltage curve overlap with the sections of strong hysteresis in the current−voltage curve (Figure 7c). Dimensional changes were measured on various samples, in a direction perpendicular to the layers. The strain amplitudes achieved vary between 3% and 6%. The red curve in Figure 8a displays a strain amplitude of ~6% measured for a sample with the layered morphology. If we compare this to the 0.1% strain amplitude measured for a nanoporous Au sample having the standard one-length-scale structure (see black curve in Figure 8a), it is concluded that the strain amplitude is boosted by a factor of almost 2 orders of magnitude due to the new morphology. We attribute the origin of these giant strains to the deformation mechanism of the layers, and we propose the following physical picture: first, expansion during opening of the scales might contribute to these large displacements. During Au electro-oxidation, anions adsorbed onto the metal surface attract a positive charge in the space-charge region[9] at the surface of the nanoporous Au, leading to relaxation of the surface atomic bonds, resulting in an expansion of the ligaments. Bulk expansion of the ligaments should result in a uniform elastic expansion up to 0.1−0.2% of the individual porous Au layers.[6,7,9,10,35] However, it is believed that due to the inhomogeneity in the stacked nanoporous Au layers (variation in thickness), the thickness of the oxide coverage formed on the nanoporous Au layers during electro-oxidation (forward anodic scan) does not scale with the thickness of these nanoporous Au layers; for example, the thickness of the oxide coverage on a 50 nm thick nanoporous Au layer is about equal to that on a 200 nm thick nanoporous Au layer. Consequently, the amount of electric charge accumulated in the space-charge region[9] at the nanoporous Au surface during electro-oxidation does not scale with the thickness of the nanoporous Au layers. As a result, two adjacent nanoporous Au layers might not evenly expand, and this might give rise to a misfit strain between adjacent nanoporous Au scales. Since the scales are locally clamped onto each other, the misfit strain can result in deflection; that is, the nanoporous Au layers deform by bending in a direction out of the plane of the layers (see Figure 8b). When the Au oxide coverage is removed during electro-reduction (reverse cathodic scan), positive charges injected in the space-charge region[9] at the metal surface are withdrawn, giving rise to strengthening of the bonds between atoms at the metal surface. This yields compressive stresses in the bulk of the ligaments and thus shortening of the ligaments. At the scale of the Au layers this causes the ligaments to shrink back to their initial shapes, the misfit strains to vanish, and the bent nanoporous Au layers to relax, giving rise to the macroscopic sample contraction.

The aforementioned giant strains are not the only consequence of the layered structure in nanoporous Au. Due to the presence of these layers, thick films can deform by bending, going as far as rolling into cylinders, as displayed in Figure 4c. These large rolling deformations cannot be achieved in nanoporous Au with uniform structure because of its highly brittle nature. In addition, when nanoporous Au with a layered structure is used as metallic muscle in a bilayer strip configuration[10] consisting of a thin solid Au and a thick porous Au layer, it was found that also the composite material experiences large charge-induced curling deformations.

Proposed Model for the Giant Strains. The bending-induced deformation mechanism is schematically displayed in Figure 8b (see also Supporting Figure S2). The layers are connected together at discrete pinning sites a distance λ apart. When charge is injected, the individual layers will expand with a strain ε_i^*, with i an index indicating the individual layers. This strain corresponds to the typical 0.1% strain amplitudes measured in conventional nanoporous Au. In the situation that all layers would respond with exactly the same actuation strain, the structure would still be compatible and no internal stress would develop. In that case the overall strain would be on the order of 0.1% in all directions (in and out of the plane of the film) and no strain enhancement out of the plane would be present.

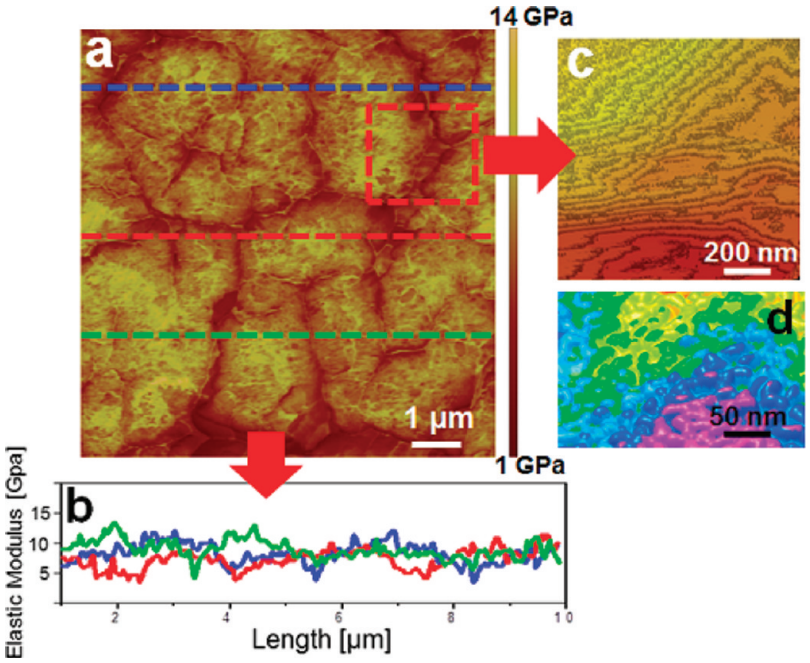

Figure 9. Elastic moduli mapping by AFM. (a) 2D quantitative mapping of the elastic modulus of nanoporous Au with a layered structure, scanned area of 10 × 10 μm^2. (b) Elastic moduli profiles taken along the blue, red, and green lines. (c) Snapshot of 3D high-resolution mapping of the elastic modulus of nanoporous Au with a layered structure. The layered pattern is discernible. (d) Snapshot of 3D high-resolution topography of nanoporous Au. Ligaments and pores are discernible.

However, local variations in the internal layer morphology as aforementioned might result in a variation in actuation strains among the nanoporous Au layers. As a result, the structure is no longer compatible, and internal stresses arise. These stresses will lead to deflection of the Au layers. To quantify this, we approximate the profile of a buckled scale with the functional form (see Figure 8b)[36,37]

$$w(x) = H \sin\left(\frac{2\pi x}{\lambda}\right) \quad (1)$$

where w is the deflection at a given location x, and H represents the maximum amplitude. The relation between the misfit strain $\Delta\varepsilon^* = \varepsilon_i - \varepsilon_{i-1}$ between two adjacent layers and the resulting deflection H can be obtained by calculating the contour length of the deformed layer:

$$\ell = \int_0^{\lambda} \sqrt{1 + \left(\frac{\partial w}{\partial x}\right)^2}\, dx \approx \lambda + \frac{\pi^2 H^2}{\lambda} \quad (2)$$

The strain required to induce this deflection is written as

$$\Delta\varepsilon^* = \frac{\ell - \lambda}{\lambda} \approx \frac{H^2\pi^2}{\lambda^2} \quad (3)$$

If t represents the average thickness of a scale (see Figure 8b), then the overall macroscopic strain can be written as $\Delta\varepsilon = (H - t)/t \approx H/t$. By substituting $H = \varepsilon t$ in eq 3, we can write the macroscopic strain in terms of the microscopic misfit strains as

$$\varepsilon \approx \frac{\sqrt{\Delta\varepsilon^*}}{\pi}\frac{\lambda}{t} \quad (4)$$

The misfit strain responsible for a macroscopic strain of 5% can be estimated by taking an average scale thickness of $t \approx 100$ nm and average lateral distance between pinning sites of $\lambda \approx 5$ μm (Figures 2c and 4d), leading to $\Delta\varepsilon^* \approx 10^{-5}$. This value is quite reasonable and represents only one percent of the actuation strain ($\sim 10^{-3}$) of the separate layers.

Dimensional changes in the electrolyte are on the order of a few micrometers, measured over a thickness of 70 μm. Therefore, they should be visible *in situ*, in an optical microscope. This was verified on a thick nanoporous Au film with scale-like morphology. When the edge of the film (cross section) was in focus, dimensional changes were observed. However, when focus was done on the surface, no lateral dimensional change of the film was observed. Instead, the surface appeared to get out of focus, which indicates an out-of plane dimensional change. These *in situ* observations are in agreement with the aforementioned argument according to which lateral displacements of the sample are converted into out-of-plane displacements. We emphasize that the out-of plane giant displacements are not associated with lateral contractions of the sample. This means that the maximum volumetric change associated with the giant strains can be approximated by $\Delta V/V \approx \Delta z/z$, where z is the out-of plane displacement in the (x,y,z) Cartesian system (see Supporting Figure S2); this corresponds to a volumetric strain amplitude of 6%.

Enhanced Work Density. The work density $W = 1/2Y\varepsilon^2$ of nanoporous Au actuator with and without layered

structure was investigated; here W, Y, and ε represent the volume work density, effective Young's modulus, and maximum strain, respectively.[38,39] The effective Young's moduli were directly measured from the two types of materials during quantitative mapping of their mechanical properties with an atomic force microscope (Bruker), in PeakForce QNM (quantitative nanomechanical mapping) imaging mode (see Methods).[40,41] A typical two-dimensional quantitative mapping of the elastic modulus of nanoporous Au with layered structure is shown in Figure 9a for a scanned area of $10 \times 10\ \mu m^2$. The corresponding elastic moduli profiles taken along the blue, red, and green lines are plotted in Figure 9b. The average elastic modulus of nanoporous Au with a layered structure was found to be ~7 GPa. Similar measurements were performed on nanoporous Au with conventional uniform porous morphology (average ligament size ~30 nm), and the corresponding average effective elastic modulus was found to be ~13 GPa, roughly double that of nanoporous Au with a layered structure. Interestingly, these two values of the effective Young's moduli are comparable with experimental data reported in the literature[42] for nanoporous Au with an average ligament size of ~30 nm. Figure 9c displays a snapshot of a three-dimensional high-resolution mapping of the elastic modulus of nanoporous Au with a layered structure; the layered pattern is discernible in this elastic modulus mapping, which indicates that the presence of the layers affects the mechanical strength. Figure 9d shows a typical three-dimensional topography of nanoporous Au as obtained from a high-resolution height mapping. Ligaments and pores are distinguishable; the differences in color are associated with differences in height.

The elastic moduli were used to investigate the work densities of the two types of nanoporous Au. Since these elastic moduli are measured at particular sites on the surface, they do not necessarily represent the exact values of the elastic moduli of the corresponding bulk nanoporous Au samples. Therefore, a comparative analysis on the work densities of the two materials was preferred, rather than going for the absolute values. The ratio between the work density of a nanoporous Au actuator with a dual microscopic length scale (volumetric strain 6%) and that of a nanoporous Au actuator with a one-length-scale porous morphology (volumetric strain 0.3%) was found to be ~215. It is concluded that the relatively low effective Young's modulus of nanoporous Au with a layered structure (compared to that of nanoporous Au with a uniform porous morphology) is largely compensated by the giant strain amplitudes. The large strains in nanoporous Au with a layered structure give rise to an enhancement of the work density of at least 2 orders of magnitude.

Finally to position this work, recently various alternatives for achieving large displacements in actuation materials have been investigated[43] and several ideas were proposed for the displacement amplification including cantilever systems, hydraulic-piston devices, and piezoelectric motors. These techniques however are not always appropriate for microscale applications.[43] Kramer *et al.*[10] have achieved large relative displacements during cantilever bending experiments, up to ~3 mm over a length of ~35−40 mm, by using a nanoporous metal strip to design a 40 mm long bilayer strip. One advantage of the actuation mechanism associated with the layered structure presented in this paper is the possibility to achieve comparable large relative displacements at smaller scales: displacements up to ~4 μm can be achieved over a thickness of ~70 μm. This approach is suitable for the current technological trends stimulated by miniaturization of devices.

CONCLUSIONS

In summary, the main findings in this paper include engineering dealloyed structures *via* the microstructure of the alloy precursor. This approach is exploited to synthesize nanoporous Au with a dual microscopic length scale structure. It is shown that the thickness of the porous layers in this structure can be controlled *via* the grain texture of the alloy precursor. The layered architecture could be exploited to enhance the functional properties of nanoporous materials. As an illustration, we show that the charge-induced strain response of nanoporous Au with a layered morphology is amplified by roughly 2 orders of magnitude.

METHODS

Strain Measurements with a Confocal Displacement Sensor. The basic operating principle of our optical displacement device is based on the differences in optical path lengths, when incoming light of a well-defined wavelength is reflected from a moving surface. The confocal displacement sensor IFS2401-0.4 Micro-Epsilon is designed to operate in air as well as in a liquid environment. During optical displacement measurements a polychromatic white light with a spot size of 10 μm is focused onto the sample surface by an integrated multilens optical system maintained out of the electrolyte, at a fixed working distance of 9 mm from the sample surface. This incoming beam of light travels in air and through the electrolyte before striking the sample surface (see Supporting Figure S1). The wavelength that is exactly in focus is reflected from the sample surface back *via* the electrolyte and air to integrated detectors, where it is further transferred *via* fiber-optic cable to an opto-electronic controller, where spectral changes are detected and processed. Changes in the spatial coordinates of the reflecting surface can then be measured with a spatial resolution of ~9 nm. The confocal displacement device was

factory calibrated (Micro-Epsilon, Germany), and the quality of the calibration was verified prior to strain measurements.

Elastic Moduli Mapping by AFM in PeakForce Imaging Mode. PeakForce QNM atomic force microscopy imaging mode has become attractive for the quantitative characterization of nanoscale materials.[40,41] This method was used in our work to estimate the effective elastic moduli of nanoporous Au with and without a layered structure during high-resolution imaging of their topography. In Peakforce Tapping mode, the sample oscillates by means of a *z*-piezo in the scanner at a lower frequency (~2 kHz) than the cantilever would oscillate in the same mode. The cantilever deflection and the *z*-piezo displacement are recorded and provide information on the deformation of the sample. This information together with the stiffness of the cantilever, the deflection sensitivity, and the tip radius was collected and processed using the Nanoscope-V controller and the Nanoscope-8 software. The determination of the elastic modulus is based on the DMT (Derjagin, Muller, Toropov) model,[41] and a good calibration is required for reliable quantitative characterization. For our measurements on nanoporous Au, the probe of choice was TAP525A, which is suitable for the determination of elastic moduli in the range of 1 to 20 GPa. The nominal spring constant and tip radius were 200 N/m and 8 nm, respectively. The deflection sensitivity was determined from a sapphire sample due to its incompressibility. The relative calibration of the spring constant was performed using a HOPG (highly oriented pyrolytic graphite) sample with a well-defined elastic modulus of 18 GPa. Measured elastic moduli (7 and 13 GPa) on our nanoporous Au samples with average ligament size of 30 nm are comparable with literature data[42] for nanoporous Au with comparable feature sizes. This means that our calibration is reliable.

Conflict of Interest: The authors declare no competing financial interest.

Acknowledgment. The authors are grateful to The Netherlands Organization for Scientific Research (NWO-the Hague, Mozaïek 2008 BOO Dossiernr: 017.005.026) and the Zernike Institute for Advanced Materials for their financial support. The authors thank P. M. Bronsveld for the master alloy preparation, E. De Jong for the investigation of the specific surface area, V. Ocelík for the EBSD, I. Hemmati and I. Furár for EBSD sample preparation, and M. Eekma for AFM measurements.

Supporting Information Available: Synthesis of the master alloys; increase in the specific surface area and its consequence for the giant strains; Figure S1 with a schematic illustration of the setup for strain measurements; Figure S2 illustrating the deformation modes in nanoporous Au with and without a layered structure. This material is available free of charge *via* the Internet at http://pubs.acs.org.

REFERENCES AND NOTES

1. Wittstock, A.; Zielasek, V.; Biener, J.; Friend, C. M.; Bäumer, M. Nanoporous Gold Catalysts for Selective Gas-Phase Oxidative Coupling of Methanol at Low Temperature. *Science* **2010**, *327*, 319–322.
2. Wittstock, A.; Biener, J.; Bäumer, M. Nanoporous Gold: a New Material for Catalytic and Sensor Applications. *Phys. Chem. Chem. Phys.* **2010**, *2*, 12919–12930.
3. Nagle, L. C.; Rohan, J. F. Nanoporous Gold Anode Catalyst for Direct Borohydride Fuel Cell. *Int. J. Hydrogen Energy* **2011**, *36*, 10319–10326.
4. Xu, C.; Xu, X.; Su, J.; Ding, Y. Research on Unsupported Nanoporous Gold Catalyst for CO Oxidation. *J. Catal.* **2007**, *252*, 243–248.
5. Lang, X. Y.; Yuan, H. T.; Iwasa, Y.; Chen, M. W. Three-Dimensional Nanoporous Gold for Electrochemical Supercapacitors. *Scr. Mater.* **2011**, *64*, 923–926.
6. Weissmüller, J.; Viswanath, R. N.; Kramer, D.; Zimmer, P.; Würschum, R.; Gleiter, H. Charge-Induced Reversible Strain in a Metal. *Science* **2003**, *300*, 312–315.
7. Jin, H. J.; Wang, X.-L.; Parida, S.; Wang, K.; Seo, M.; Weissmüller, J. Nanoporous Au-Pt Alloys as Large Strain Electrochemical Actuators. *Nano Lett.* **2010**, *10*, 187–194.
8. Biener, J.; Wittstock, A.; Zepeda-Ruiz, L. A.; Biener, M. M.; Zielasek, V.; Kramer, D.; Viswanath, R. N.; Weissmüller, J.; Bäumer, M.; Hamza, A. V. Surface-Chemistry-Driven Actuation in Nanoporous Gold. *Nat. Mater.* **2009**, *8*, 47–51.
9. Jin, H. J.; Weissmüller, J. Bulk Nanoporous Metal for Actuation. *Adv. Eng. Mater.* **2010**, *12*, 714–723.
10. Kramer, D.; Viswanath, R. N.; Weissmüller, J. Surface-Stress Induced Macroscopic Bending of Nanoporous Gold Cantilevers. *Nano Lett.* **2004**, *4*, 793–796.
11. Yavuz, M. S.; Cheng, Y.; Chen, J.; Cobley, C. M.; Zhang, Q.; Rycenga, M.; Xie, J.; Kim, C.; Song, K. H.; Schwartz, A. G.; *et al.* Gold Nanocages Covered by Smart Polymers for Controlled Release with Near-Infrared Light. *Nat. Mater.* **2009**, *8*, 935–939.
12. Au, L.; Zheng, D.; Zhou, F.; Li, Z.-Y.; Li, X.; Xia, Y. A Quantitative Study on the Photothermal Effect of Immuno Gold Nanocages Targeted to Breast Cancer Cells. *ACS Nano* **2008**, *2*, 1645–1652.
13. Gittard, S. D.; Pierson, B. E.; Ha, C. M.; Max, Wu, C.-A.; Narayan, R. J.; Robinson, D. B. Supercapacitive Transport of Pharmacologic Agents Using Nanoporous Gold Electrodes. *Biotechnol. J.* **2010**, *5*, 192–200.
14. Meng, F.; Ding, Y. Sub-Micrometer-Thick all-Solid-State Supercapacitors with High Power and Energy Densities. *Adv. Mater.* **2011**, *23*, 4098–4102.
15. Lang, X.; Zhang, L.; Fujita, T.; Ding, Y.; Chen, M. Three-Dimensional Bicontinuous Nanoporous Au/Polyaniline Hybrid Films for High-Performance Electrochemical Supercapacitors. *J. Power Sources* **2012**, *197*, 325–329.
16. Parida, S.; Kramer, D.; Volkert, C. A.; Rösner, H.; Erlebacher, J.; Weissmüller, J. Volume Change During the Formation of Nanoporous Gold by Dealloying. *Phys. Rev. Lett.* **2006**, *97*, 035504.
17. Erlebacher, J.; Aziz, M. J.; Karma, A.; Dimitrov, N.; Sieradzki, K. Evolution of Nanoporosity in Dealloying. *Nature* **2001**, *410*, 450–453.
18. Erlebacher, J.; Sieradzki, K. Pattern Formation During Dealloying. *Scr. Mater.* **2003**, *49*, 991–996.
19. Snyder, J.; Erlebacher, J. Kinetics of Crystal Etching Limited by Terrace Dissolution. *J. Electrochem. Soc.* **2010**, *157*, 125–130.
20. Detsi, E.; De Jong, E.; Zinchenko, A.; Vuković, Z.; Vuković, I.; Punzhin, S.; Loos, K.; Ten Brinke, G.; De Raedt, H. A.; Onck, P. R.; *et al.* On the Specific Surface Area of Nanoporous Materials. *Acta Mater.* **2011**, *59*, 7488–7497.
21. Detsi, E.; Punzhin, P.; Onck, P. R.; De Hosson, J. T. M. Direct Synthesis of Metal Nanoparticles with Tunable Porosity. *J. Mater. Chem.* **2012**, *22*, 4588–4591.
22. Biener, J.; Hodge, A. M.; Hayes, J. R.; Volkert, C. A.; Zepeda-Ruiz, L. A.; Hamza, A. V.; Abraham, F. F. Size Effects on the Mechanical Behavior of Nanoporous Au. *Nano Lett.* **2006**, *6*, 2379–2382.
23. Detsi, E.; Van de Schootburgge, M.; Punzhin, S.; Onck, P. R.; De Hosson, J. T. M. On Tuning the Morphology of Nanoporous Gold. *Scr. Mater.* **2011**, *64*, 319–322.
24. Hodge, A. M.; Biener, J.; Hayes, J. R.; Bythrow, P. M.; Volkert, C. A.; Hamza, A. V. Scaling Equation for Yield Strength of Nanoporous Open-Cell Foams. *Acta Mater.* **2007**, *55*, 1343–1349.
25. Qian, L. H.; Chen, M. W. Ultrafine Nanoporous Gold by Low-Temperature Dealloying and Kinetics of Nanopore Formation. *Appl. Phys. Lett.* **2007**, *91*, 083105.
26. Ding, Y.; Kim, Y. J.; Erlebacher, J. Nanoporous Gold Leaf: "Ancient Technology. *Adv. Mater.* **2004**, *16*, 1897–1900.
27. Morrish, R.; Dorame, K.; Muscat, A. F. Formation of Nanoporous Au by Dealloying AuCu Thin Films in HNO_3. *Scr. Mater.* **2011**, *64*, 856–859.
28. Hakamada, M.; Mabuchi, M. Mechanical Strength of Nanoporous Gold Fabricated by Dealloying. *Scr. Mater.* **2007**, *56*, 1003–1006.
29. Volkerta, C. A.; Lilleodden, E. T.; Kramer, D.; Weissmüller, J. Approaching the Theoretical Strength in Nanoporous Au. *Appl. Phys. Lett.* **2006**, *89*, 061920.

30. Jin, H. J.; Parida, S.; Kramer, D.; Weissmüller, J. Sign-Inverted Surface Stress-Charge Response in Nanoporous Gold. *Surf. Sci.* **2008**, *602*, 3588–3594.
31. Sun, Y.; Balk, T. J. A Multi-Step Dealloying Method to Produce Nanoporous Gold with No Volume Change and Minimal Cracking. *Scr. Mater.* **2008**, *58*, 727–730.
32. Kim, S. H.; Erb, U.; Aust, K. T.; Palumbo, G. Grain Boundary Character Distribution and Intergranular Corrosion Behavior in High Purity Aluminum. *Scr. Mater.* **2001**, *44*, 835–839.
33. Conway, B. E. Electrochemical Oxide Film Formation at Noble Metals As a Surface-Chemical Process. *Prog. Surf. Sci.* **1995**, *49*, 331–452.
34. Burke, L. D.; Nugent, P. F. The Electrochemistry of Gold: I The Redox Behaviour of the Metal in Aqueous Media. *Gold Bull.* **1997**, *30*, 43–53.
35. Detsi, E.; Chen, Z. G.; Vellinga, W. P.; Onck, P. R.; De Hosson, J. T. M. Reversible Strain by Physisorption in Nanoporous Gold. *Appl. Phys. Lett.* **2011**, *99*, 083104.
36. Annabattula, R. K.; Veenstra, J. M.; Mei, Y. F.; Schmidt, O. G.; Onck, P. R. Self-Organization of Linear Nanochannel Networks. *Phys. Rev. B* **2010**, *81*, 224114.
37. Edmondson, S.; Frieda, K.; Comrie, J. E.; Onck, P. R.; Huck, W. T. S. Buckling in Quasi-2D Polymers. *Adv. Mater.* **2006**, *18*, 724–728.
38. Baughman, R. H.; Cui, C.; Zakhidov, A. A.; Iqbal, Z.; Barisci, J. N.; Spinks, G. M.; Wallace, G. G.; Mazzoldi, A.; De Rossi, D.; Rinzler, A. G.; Jaschinski, O.; *et al*. Carbon Nanotube Actuators. *Science* **1999**, *284*, 1340.
39. Zhang, Q. M.; Bharti, V.; Zhao, X. Giant Electrostriction and Relaxor Ferroelectric Behavior in Electron-Irradiated Poly(vinylidene fluoride-trifluoroethylene) Copolymer. *Science* **1998**, *280*, 2101.
40. Schön, P.; Bagdi, K.; Molnár, K.; Markus, P.; Pukánszky, B.; Vancso, G. J. Quantitative Mapping of Elastic Moduli at the Nanoscale in Phase Separated Polyurethanes by AFM. *Eur. Polym. J.* **2011**, *47*, 692–698.
41. Cranston, E. D.; Eita, M.; Johansson, E.; Netrval, J.; Salajková, M.; Arwin, H.; Wågberg, L. Determination of Young's Modulus for Nanofibrillated Cellulose Multilayer Thin Films Using Buckling Mechanics. *Biomacromolecules* **2011**, *12*, 961–969.
42. Mathur, A.; Erlebacher, J. Size Dependence of Effective Young's Modulus of Nanoporous Gold. *Appl. Phys. Lett.* **2007**, *90*, 061910.
43. Conway, N. J.; Traina, Z. J.; Kim, S. G. A Strain Amplifying Piezoelectric MEMS Actuator. *J. Micromech. Microeng.* **2007**, *17*, 781.